J Adv Ceram

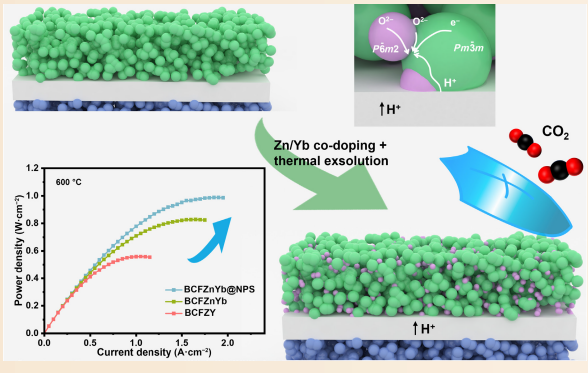
Research Article

Cation-driven charge modulation and *in-situ* exsolved nanoparticles enable a self-assembled cathode for proton ceramic solid oxide cells

Mengen Shao[1], Xinyu Zhao[2,3], Chaowei Tang[1], Yuling Yuan[1], Guangming Yang[4], Yan Chen[5], Jaroslaw Milewski[6], Tao Hong[7], Yu Liu[3], Zuoqing Liu[1,✉], Youmin Guo[1,✉]

Cite this article: Shao M, Zhao X, Tang C, et al. *J Adv Ceram* 2026, **15**(8): 9221340. https://doi.org/10.26599/JAC.2026.9221340

ABSTRACT: Protonic ceramic fuel cells (PCFCs) offer considerable potential for clean and efficient energy conversion at intermediate temperatures. However, their application is constrained by the trade-off between insufficient electrode activity and limited operational durability. Here, we develop a Zn/Yb B-site codoping strategy combined with temperature-induced nanoparticle exsolution to construct a triple-conducting cathode. This approach introduces cation-driven charge modulation that enhances ionic diffusion and electronic conduction, while the exsolved secondary $BaCoO_{3-\delta}$ phase plays a pivotal role in increasing the density of active sites, optimizing interfacial charge transfer, and synergistically promoting oxygen reduction reaction (ORR) kinetics. Zn/Yb codoping redistributes the local charge density, weakens metal–oxygen bonds, and reduces the energy required for oxygen vacancy formation, promoting oxygen vacancy generation. The increased oxygen vacancy concentration facilitates surface oxygen activation and lattice hydration, enhancing oxygen–ion and proton transport. Meanwhile, enhanced d–p orbital hybridization improves the electronic conductivity and accelerates charge transfer kinetics. In addition, the optimized alkaline–earth sites suppress carbonate formation, thereby imparting excellent CO_2 tolerance. As a result, the optimized cathode delivers a peak power density of 0.99 W·cm^{-2} at 600 °C and stable operation over 100 h, with a polarization resistance of 0.110 Ω·cm^2 under 20% H_2O-air. This work provides a novel strategy for the optimization of activity, conductivity, and stability in PCFC cathodes.



KEYWORDS: solid oxide cells (SOCs); cathode; triple conductor; oxygen vacancy; CO_2 tolerance

1 Introduction

Solid oxide cells (SOCs) are promising devices for efficient and clean energy conversion, owing to their fuel flexibility, high efficiency, and all-solid-state architecture that mitigates issues related to corrosion and electrolyte leakage [1,2]. However, conventional SOCs typically operate at high temperatures (800–1000 °C), which causes several critical issues, including rapid degradation, slow start-up, and high costs. These limitations have hindered their widespread commercialization [3]. To overcome these challenges, protonic ceramic fuel cells (PCFCs) have been developed as a promising alternative. They employ proton-conducting electrolytes, such as $BaZr_{0.1}Ce_{0.7}Y_{0.1}Yb_{0.1}O_{3-\delta}$ (BZCYYb), and operate at reduced temperatures (400–700 °C), benefitting from the lower activation energy required for proton transport [4–6]. This intermediate-temperature operation mitigates high-temperature degradation processes (e.g., oxidation and phase separation) and reduces the dependence on costly thermal-resistant materials. Moreover, the formation of water at the cathode side avoids fuel dilution, thereby enhancing fuel utilization efficiency [7,8]. Nevertheless, the presence of water vapor and intermediate operation temperatures imposes new requirements on cathode materials, which must exhibit high stability under humid conditions and resistance to CO_2 poisoning

[1] School of Materials Science and Engineering, Anhui University, Hefei 230601, China. [2] School of Energy and Mechanical Engineering, Nanjing Normal University, Nanjing 210023, China. [3] Energy Storage Research and Development Center, Institute of Engineering Thermophysics, Chinese Academy of Sciences, Beijing 100190, China. [4] College of Chemical Engineering, Nanjing Tech University, Nanjing 211800, China. [5] Guangdong Provincial Key Laboratory of Solid Wastes Pollution Control and Recycling, School of Environment and Energy, South China University of Technology, Guangzhou 510006, China. [6] Faculty of Power and Aeronautical Engineering, Warsaw University of Technology, Warsaw 00-661, Poland. [7] School of Materials Science and Engineering, Hefei University of Technology, Hefei 230009, China.

✉ Corresponding authors. E-mail: Z. Liu, zuoqing0605@ahu.edu.cn; Y. Guo, youminguo@ahu.edu.cn

Received: April 25, 2026; Revised: May 27, 2026; Accepted: June 18, 2026

© The Author(s) 2026. This is an open access article under the terms of the Creative Commons Attribution 4.0 International License (CC BY 4.0, http://creativecommons.org/licenses/by/4.0/).

[9,10]. Furthermore, unlike mixed ionic–electronic conducting (MIEC) cathodes used in conventional SOCs, an ideal PCFC cathode should possess triple ($H^+/O^{2-}/e^-$) conductivity to extend the active region for the oxygen reduction reaction (ORR) throughout the electrode bulk. Despite increasing research attention, the performance and durability of PCFC cathodes in the intermediate-temperature range remain inadequate, limiting their commercial viability [11–13]. More critically, sluggish cathode reaction kinetics remain a key bottleneck limiting the large-scale commercialization of PCFCs [14,15].

In recent decades, extensive efforts have been devoted to addressing the sluggish ORR kinetics of PCFC cathodes. Conventional approaches include surface modification (e.g., infiltration and mechanical mixing) and compositional/defect engineering to construct triple-conducting ($H^+/O^{2-}/e^-$) cathodes, thereby extending ORR activity from the triple-phase boundaries to the electrode bulk. For example, Yao *et al.* [16] modified $La_{0.6}Sr_{0.4}Co_{0.2}Fe_{0.8}O_{3-\delta}$ (LSCF) via infiltration of $Pr_2Ni_{0.5}Co_{0.5}O_{4-\delta}$ (PNC), introducing abundant oxygen vacancies to accelerate oxygen adsorption, dissociation, and surface exchange while facilitating proton transport to compensate for its limited proton conductivity. However, infiltration is complex and costly, and nanoparticles tend to agglomerate or detach, limiting stability and scalability. Recently, self-assembled cathodes have emerged as an effective strategy to overcome these limitations [17]. Their architectures enable optimized charge redistribution and oxygen vacancy concentration, enhancing ORR activity while alleviating nonuniform active site distribution and weak interfacial adhesion. For instance, Qi *et al.* [18] utilized the acid–base interaction between $BaCo_{0.4}Fe_{0.4}Zr_{0.1}Y_{0.1}O_{3-\delta}$ (BCFZY) and H_2O/CO_2 to form $BaCoO_3$–$BaCO_3$ nanocomposites, which transformed into a dense BCFZY coating after calcination; the resulting hierarchical cathode exhibited low ORR polarization resistance. However, this approach reveals the limited H_2O/CO_2 tolerance of BCFZY and does not fundamentally improve the intrinsic stability of the host lattice. Park *et al.* [19] reported that alkali–metal doping in $BaCo_{0.4}Fe_{0.4}Zr_{0.18}Y_{0.02}O_{3-\delta}$ induces water-mediated exsolution of BaO_x nanoparticles under humid air, optimizing proton uptake, oxygen vacancy formation, and proton migration and thereby enhancing ORR/oxygen evolution reaction (OER) bifunctional activity and reversible performance. Although partial doping modifications were applied to the host lattice, stability under CO_2-containing conditions was still overlooked. Moreover, compared with the water-mediated strategy, our temperature-driven exsolution approach exhibits several distinct advantages. First, exsolution is activated directly by thermal treatment at 950 °C in conventional air without introducing external reactive media such as water vapor, which significantly simplifies the fabrication process and improves scalability. Second, this strategy avoids the need for dedicated humidification systems. Third, potential electrode–electrolyte interfacial side reactions associated with prolonged steam treatment are circumvented.

In this work, we design a host–lattice-focused strategy based on synergistic Zn/Yb B-site codoping combined with a simple temperature-induced exsolution under an optimal thermal window. In this design, Zn^{2+} replaces Zr^{4+} for size compatibility and oxygen vacancy generation via charge compensation, while Yb^{3+} replaces Y^{3+} for electronic modulation. A self-assembled triple-conducting cathode with a nominal composition of $BaCo_{0.4}Fe_{0.4}Zn_{0.1}Yb_{0.1}O_{3-\delta}$ is synthesized via a sol–gel method. Upon thermal induction, this cathode forms hexagonal $BaCoO_{3-\delta}$ nanoparticles (secondary phase) on the surface of the cubic perovskite matrix, forming the composite denoted as BCFZnYb@NPs (where NPs refer to these *in situ* exsolved nanoparticles), which increases the density of electrocatalytic active sites and significantly enhances ion transport rates. Furthermore, the optimized cation coordination environment reduces the energy barrier for oxygen vacancy formation, increases the effective oxygen vacancy concentration, and improves the electronic transport capability. The cathode exhibits enhanced hydration capability under wet air, promoting ORR kinetics; a reduced density of surface alkaline–earth sites endows it with excellent CO_2 tolerance. A single cell based on the BCFZnYb@NPs cathode and BZCYYb electrolyte achieves a peak power density of 0.99 $W \cdot cm^{-2}$ at 600 °C and stable operation for over 100 h. This study proposes a composite electrode design strategy combining temperature induction and cation driving, realizing the synergistic integration of high conductivity, excellent catalytic activity, and outstanding stability, which provides a feasible pathway for the development of high-performance intermediate-temperature PCFCs.

2 Experimental

2.1 Powder synthesis

The cathode materials BCFZnYb@NPs, $Ba_{0.95}Co_{0.4}Fe_{0.4}Zn_{0.1}Yb_{0.1}O_{3-\delta}$ (BCFZnYb), BCFZY, and the electrolyte powder BZCYYb were synthesized via the sol–gel method. Metal nitrate precursors $Ba(NO_3)_2$, $Co(NO_3)_2 \cdot 6H_2O$, $Fe(NO_3)_3 \cdot 9H_2O$, $Zr(NO_3)_4 \cdot 5H_2O$, $Y(NO_3)_3 \cdot 6H_2O$, $Yb(NO_3)_3 \cdot 5H_2O$, $Zn(NO_3)_2 \cdot 6H_2O$, and $Ce(NO_3)_3 \cdot 6H_2O$ were used as starting materials. Taking the synthesis of BCFZnYb@NPs as an example, stoichiometric amounts of $Ba(NO_3)_2$, $Co(NO_3)_2 \cdot 6H_2O$, $Fe(NO_3)_3 \cdot 9H_2O$, $Zn(NO_3)_2 \cdot 6H_2O$, and $Yb(NO_3)_3 \cdot 5H_2O$ were dissolved in deionized water at 90 °C with continuous stirring. Ethylenediaminetetraacetic acid (EDTA) and citric acid (CA) were added as chelating agents, with a molar ratio of EDTA : CA : total metal ions = 1 : 2 : 1. The pH was adjusted to 7–8 using ammonium hydroxide aqueous solution, resulting in a transparent brown solution. After stirring until the mixture became viscous, it was dried at 240 °C for 6 h and then calcined in air at 950 °C for 2 h (heating rate: 5 $°C \cdot min^{-1}$) to obtain the perovskite powder. BCFZY and BCFZnYb were prepared similarly, while BZCYYb required calcination at 1000 °C for 5 h. To eliminate the influence of different cathode calcination temperatures on grain size, specific surface area, and oxygen vacancy concentration, a single-phase BCFZnYb sample with adjusted A/B-site stoichiometry was deliberately designed and calcined at the same temperature of 950 °C as the control sample [20]. For the anode, BZCYYb electrolyte powder was mixed with NiO and polyvinyl butyral (PVB) at a mass ratio of 12:8:1, ball-milled in ethanol for 2 h, and dried under a sodium lamp to form the anode powder.

2.2 Cell fabrication

An anode-supported single cell with the structure of NiO–BZCYYb|BZCYYb|BCFZnYb@NPs and a symmetric cell with the configuration of BCFZnYb@NPs|BZCYYb|BCFZnYb @NPs were fabricated. The anode-supported single cell was prepared via a co-pressing technique: 0.35 g of anode powder was first pressed into a disc, after which 0.02 g of electrolyte powder was uniformly distributed over the prepressed anode disc and copressed. The resulting green body was sintered in air at 1450 °C (heating rate: 5 $°C \cdot min^{-1}$) to obtain a half-cell with a dense thin electrolyte membrane. For the cathode layer, 1 g of cathode powder was dispersed in a mixture of isopropanol (10 mL), ethylene glycol (2 mL), and glycerol (0.6 mL). The mixture was

ball-milled for 2 h to form a homogeneous cathode ink. The ink was uniformly spray-coated onto the electrolyte side of the half-cell to form a trilayered structure, which was then sintered in air at 950 °C for 2 h (heating rate: 5 °C·min^{-1}). Finally, silver paste was brushed onto the cathode surface to serve as a current collector. It is worth noting that the cathode ink was deposited exclusively on the central region of the electrolyte.

The symmetric cell was fabricated by dry-pressing 0.4 g of electrolyte powder into a disc. Cathode ink was spray-coated onto both sides of the electrolyte disc, followed by sintering in air at 950 °C for 2 h (heating rate: 5 °C·min^{-1}). Silver paste was similarly applied to both electrode surfaces for current collection.

2.3 Characterization

The synthesized materials and fabricated cells were systematically characterized using multiple analytical techniques. X-ray diffraction (XRD) analysis was performed on a 9 kW diffractometer (SMARTLAB, Rigaku, Japan) to identify crystalline phases by comparison with JCPDS PDF standards. Rietveld refinement was subsequently conducted to verify structural accuracy. Microstructural analysis of the powders was carried out using a cold field-emission scanning electron microscope (FE-SEM; Carl Zeiss Sigma 500, Zeiss, Germany). Before imaging, samples were sputter-coated with a thin layer of gold. Surface chemical states and oxygen vacancy content were analyzed via an X-ray photoelectron spectrometer (XPS; ESCALAB 250Xi, Thermo Fisher Scientific, USA). Spectral deconvolution was performed using XPS PEAK 4.1 software. Oxygen temperature-programmed desorption (O_2-TPD) experiments were conducted using an analyzer (ChemiMaster 8320, Quantachrome Instruments, USA). The samples were first pretreated in 30 sccm N_2 by heating to 800 °C at a rate of 10 °C·min^{-1} and holding for 60 min to remove surface impurities. After rapid cooling to 60 °C, the gas was switched to a 30 sccm 4% O_2/He mixture for adsorption at the same temperature for 60 min, followed by purging with 30 sccm pure He for 30 min to remove physically adsorbed oxygen species. Subsequently, TCD detection was initiated and maintained throughout, and the temperature was increased to 1000 °C at 10 °C·min^{-1} to complete the programmed desorption analysis. A thermogravimetric analyzer (TG; Netzsch TG 209 F3 Tarsus, Netzsch, Germany) was used to monitor mass changes during thermal treatment. The measurements were conducted in air with a heating rate of 10 °C·min^{-1}. CO_2–temperature-programmed desorption (CO_2-TPD) analysis was performed using an instrument (AutoChem II 2920, Micromeritics, USA). Approximately 100 mg of sample was pretreated under Ar flow at 800 °C for 1 h to remove surface contaminants. The sample was then exposed to a 1% CO_2-Ar mixture at 100 °C for 30 min for adsorption. TPD was carried out from room temperature to 800 °C at a heating rate of 10 °C·min^{-1} under Ar flow. A transmission electron microscope (TEM; JEM-F200, JEOL, Japan) was operated at an acceleration voltage of 200 kV. High-resolution lattice images and interplanar spacing analysis were obtained and processed using DM3 software. Electrochemical impedance spectroscopy (EIS) was performed using a Solartron 1260 over a frequency range of 10^{-1}–10^{6} Hz. Polarization resistance (R_p) and area-specific resistance (ASR = $R_p \times S/2$) were derived from the electrochemical impedance spectroscopy (EIS) data. The distribution of relaxation times (DRT) analysis was conducted using the open-source DRTtools toolbox. Radial basis function discretization combined with Tikhonov regularization was employed to deconvolute the EIS data into a series of relaxation processes with distinct characteristic frequencies, while the optimal regularization parameter was determined according to the L-curve criterion [21]. Single-cell performance was evaluated by measuring the power density between 500 and 700 °C using a source meter (Keithley 2420, Keithley, USA). The cathode was exposed to ambient air, while dry H_2 was supplied to the anode at a flow rate of 80 mL·min^{-1}. The effective cathode area was 0.4 cm^2.

2.4 Computational methods

First-principles calculations were carried out within the framework of density functional theory (DFT), as implemented in the Vienna *Ab initio* Simulation Package (VASP) [22,23]. The projector augmented-wave (PAW) method was used to describe the interactions between valence electrons and ionic cores. The exchange-correlation energy was treated using the generalized gradient approximation (GGA) in the Perdew–Burke–Ernzerhof (PBE) parameterization [24,25]. To accurately describe the on-site Coulomb interactions of transition-metal ions, the rotationally invariant DFT+U approach was applied, with effective Hubbard U values of 3.3 and 4.0 eV applied to the Co 3d and Fe 3d states, respectively [19]. To represent the actual stoichiometry of BCFZY and BCFZnYb@NPs-H (the perovskite host phase of BCFZnYb@NPs), 135-atom supercells were constructed, while a 134-atom supercell was used for BCFZnYb. The atomic compositions of the BCFZY, BCFZnYb@NPs-H, and BCFZnYb supercell models are $Ba_{27}Co_{10}Fe_{11}Zr_3Y_3O_{81}$, $Ba_{27}Co_{10}Fe_{11}Zn_3Yb_3O_{81}$, and $Ba_{26}Co_{10}Fe_{11}Zn_3Yb_3O_{81}$, respectively. Special quasirandom structures (SQS) were employed to construct $3 \times 3 \times 3$ supercells, in which the local atomic arrangement approximates the statistical distribution of an ideal random solid solution by optimizing the correlation functions of atomic pairs and multibody clusters, thereby effectively describing chemical disorder under periodic boundary conditions. During model construction, 5000 annealing steps were performed to sufficiently explore the configurational space, while the dopant atoms were intentionally separated as far as possible to suppress artificial short-range clustering induced by the finite supercell size. The representative configuration with the lowest total energy and highest structural stability among multiple random structures was finally selected for subsequent calculations. A plane-wave energy cutoff of 500 eV was used for all calculations. Structural relaxations were performed until the total energy and atomic forces converged within thresholds of 1×10^{-5} and 0.05 eV·Å^{-1}, respectively. The Brillouin zone was sampled using a $3 \times 3 \times 3$ Monkhorst–Pack *k*-point grid centered at the Γ point.

The oxygen vacancy formation energy (E_{vac}) was calculated by removing one oxygen atom from various lattice sites within the constructed supercell models. E_{vac} was computed via Eq. (1):

$$E_{vac} = E(A_nB_nC_{3n-1}) + \mu_O - E(A_nB_nC_{3n}) \quad (1)$$

where A, B, and C denote the A-site cation, B-site cation, and oxygen atom, respectively, and n is the number of formula units in the constructed supercell. $E(A_nB_nC_{3n})$ is the total energy of the fully relaxed pristine perovskite supercell, $E(A_nB_nC_{3n-1})$ refers to the total energy of the same supercell containing one oxygen vacancy, and μ_O denotes the chemical potential of an oxygen atom. In this study, the oxygen chemical potential was referenced to half the total energy of an isolated O_2 molecule, yielding a value of −4.89 eV per atom.

3 Results and discussion

Figure 1(a) presents the XRD patterns of the as-synthesized

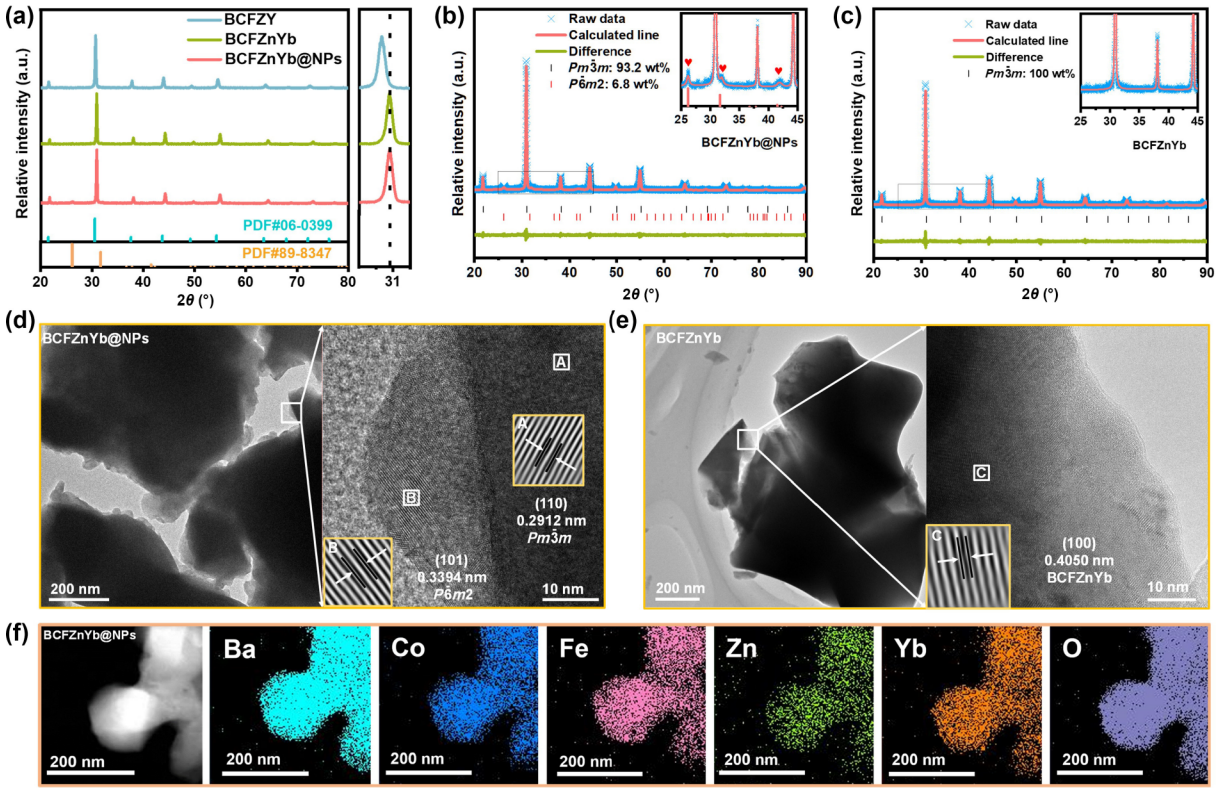


Fig. 1 (a) XRD patterns of BCFZY, BCFZnYb, and BCFZnYb@NPs powders. Rietveld refinement profiles of (b) BCFZnYb@NPs and (c) BCFZnYb. (d) HR-TEM image of BCFZnYb@NPs powder and magnifications of indicated regions A and B. (e) HR-TEM image of BCFZnYb powder and a magnification of indicated region C. (f) EDX mapping results of BCFZnYb@NPs composite.

BCFZnYb@NPs, BCFZnYb, and BCFZY powders. To eliminate the influence of sintering temperature, the A/B-site stoichiometry was adjusted to obtain a single-phase BCFZnYb at a sintering temperature of 950 °C. All samples exhibit sharp diffraction peaks, indicating high crystallinity. The main diffraction peak of BCFZnYb@NPs shifts to a higher angle than that of BCFZY, suggesting lattice contraction. This contraction is primarily attributed to the partial loss of A-site Ba^{2+} (1.61 Å) due to second-phase precipitation, rather than B–site substitution, given the similar ionic radii of Zr^{4+} (0.72 Å)/Zn^{2+} (0.74 Å) and Y^{3+} (0.90 Å)/Yb^{3+} (0.86 Å). This interpretation is supported by a similar peak shift observed in the Ba-deficient BCFZnYb. It should also be noted that the reduced valence states of B-site Co and Fe induced by Zn/Yb codoping, as confirmed by the XPS results discussed below, would generally tend to induce slight lattice expansion. Therefore, the experimentally observed net lattice contraction indicates that A-site Ba deficiency and the associated oxygen vacancy formation dominate the structural evolution. Such lattice contraction is expected to facilitate bulk proton transport, thereby enhancing the reaction kinetics.

Notably, the BCFZnYb@NPs powder forms a dual-phase structure during powder synthesis, consisting of a cubic perovskite matrix and a secondary hexagonal $BaCoO_{3-\delta}$ phase. To identify the phase composition, Rietveld refinement was conducted on the XRD patterns (Figs. 1(b), 1(c), and Figure S1 in the Electronic Supplementary Material (ESM)). The refinements confirm that both BCFZY ($Pm\bar{3}m$ space group, where a represents the cubic lattice parameter, a = 4.12 Å) and BCFZnYb ($Pm\bar{3}m$ space group, a = 4.09 Å) retain single-phase cubic perovskite structures. In contrast, BCFZnYb@NPs consist of two distinct phases: a major cubic perovskite phase ($Pm\bar{3}m$ space group, a = 4.10 Å, 93.2 wt%) and a minor hexagonal phase ($P\bar{6}m2$ space group, where a and b represent the in-plane lattice parameters and c represents the out-of-plane lattice parameter, $a = b$ = 5.60 Å, c = 4.79 Å, 6.8 wt%). The three strongest peaks of the minor phase correspond well with $BaCoO_{3-\delta}$ (PDF#89-8347). The alignment of the main diffraction peaks with those of BCFZnYb further suggests that the dominant phase in BCFZnYb@NPs is structurally analogous to BCFZnYb. This dual-phase configuration was further confirmed by high-resolution transmission electron microscopy (HR-TEM) (Figs. 1(d) and S2 in the ESM). Fast Fourier transform (FFT) and inverse FFT (iFFT) analyses reveal interplanar spacings of 0.2912 and 0.3394 nm, corresponding to the (110) plane of the cubic perovskite phase and the (101) plane of the hexagonal $BaCoO_{3-\delta}$ phase, respectively. For comparison, the single-phase BCFZnYb exhibits an interplanar spacing of 0.4050 nm, indexed to the (100) plane (Fig. 1(e)). These measured values agree well with the lattice parameters derived from XRD Rietveld refinement. Furthermore, energy-dispersive X-ray (EDX) elemental mapping (Fig. 1(f)) confirms the successful incorporation and homogeneous distribution of Zn and Yb at the probed length scale.

As shown in Fig. S3 in the ESM, the exsolution of $BaCoO_{3-\delta}$ exhibits a typical temperature-dependent behavior. No diffraction peaks of $BaCoO_{3-\delta}$ are observed in the XRD patterns of BCFZnYb@NPs precursors sintered at 900 and 1000 °C, whereas this phase appears only in the sample sintered at 950 °C. Owing to $BaCoO_{3-\delta}$ exsolution, the main XRD peaks of the 950 °C sample shift to higher angles compared with those at other temperatures, indicating lattice contraction. Scanning electron microscopy (SEM) further confirms the temperature-induced exsolution: samples sintered at 900 and 1000 °C exhibit smooth surfaces, while distinct exsolved nanoparticles are observed on the surface of the 950 °C sample, consistent with HR-TEM observations. At 900 °C, the $BaCo_{0.4}Fe_{0.4}Zn_{0.1}Yb_{0.1}O_{3-\delta}$ matrix remains within a thermodynamically stable single-phase region, where the lattice maintains relatively high solubility for Ba and Co species, and the

system energy is insufficient to overcome the phase-separation threshold. Meanwhile, the cation diffusion kinetics together with the oxygen vacancy concentration are inadequate to support exsolution, thereby preventing the formation of the $BaCoO_{3-\delta}$ secondary phase. When the temperature increases to 950 °C, the matrix enters a metastable regime. The increased oxygen vacancy concentration and local compositional fluctuation destabilize the lattice and trigger spontaneous phase separation. Under these conditions, Ba and Co species segregate and nucleate at the surface, leading to the formation of the $BaCoO_{3-\delta}$ secondary phase. Thus, 950 °C corresponds to an optimal metastable decomposition window where exsolution is most pronounced. At 1000 °C, the disappearance of $BaCoO_{3-\delta}$ does not indicate suppressed exsolution but rather a high-temperature-induced reversible dissolution. The elevated temperature significantly increases the solid solubility of Ba and Co species within the perovskite lattice, allowing the segregated components to be reincorporated into the host structure. Consequently, the secondary phase loses its thermodynamic stability, and the system returns to a stable single-phase state [26]. Furthermore, as shown in Fig. S4 in the ESM, $BaCoO_{3-\delta}$ exsolution at 950 °C was reproducibly achieved in three independently synthesized BCFZnYb@NPs samples.

As shown in Fig. S5 in the ESM, the average particle diameter (AD) of the exsolved nanoparticles in the sample sintered at 950 °C is 29.67 nm. Furthermore, since the cathode material must be sintered at 950 °C for 2 h to ensure adhesion to the electrolyte, BCFZnYb@NPs were subjected to the same resintering treatment. As shown in the XRD patterns in Fig. S6 in the ESM, the secondary phase remained detectable after resintering at 950 °C for 2 h.

The concentration of oxygen vacancies and the oxidation state of B-site transition metals in perovskite-based air electrodes are critical factors governing the triple conductivity (e^-, H^+, and O^{2-}) of PCFCs. Specifically, a higher oxygen vacancy concentration facilitates oxygen adsorption on the electrode surface and enhances the oxygen-ion diffusion coefficient, thereby accelerating ion transport to active sites and improving the ORR kinetics. To systematically compare the oxygen vacancy concentrations in BCFZnYb@NPs, BCFZnYb, and BCFZY, we employed multiple complementary techniques, including XPS, TG analysis, and O_2-TPD. As depicted in Fig. 2(a), the O 1s XPS spectra of three materials were deconvoluted into four distinct peaks, assigned to physically adsorbed H_2O (highest binding energy), adsorbed oxygen species (OH^-/O_2), highly oxidized oxygen (O_2^{2-}/O^-), and lattice oxygen (O^{2-}) [27]. The ratio of lattice oxygen to adsorbed oxygen (O_{lat}/O_{ads}), where O_{ads} encompasses H_2O, OH^-/O_2, and O_2^{2-}/O^- species, serves as a quantitative indicator of oxygen vacancy concentration: a lower ratio O_{lat}/O_{ads} corresponds to a higher concentration of oxygen vacancies [28,29]. BCFZY exhibits the highest O_{lat}/O_{ads} ratio (27.7%), while the Zn/Yb codoped materials show significantly lower values: 22.2% for single-phase BCFZnYb and 13.2% for dual-phase BCFZnYb@NPs. This progressive reduction suggests that Zn/Yb codoping effectively

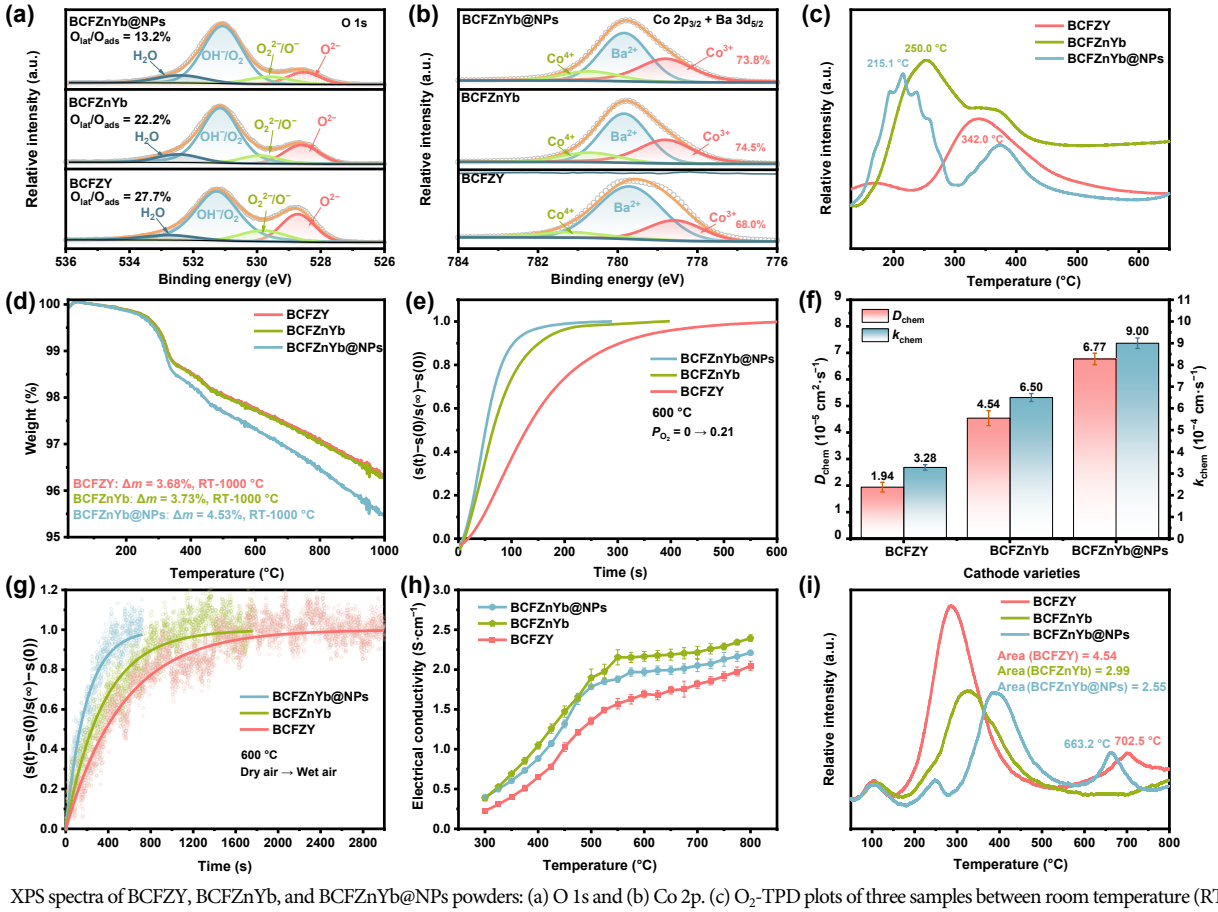


Fig. 2 XPS spectra of BCFZY, BCFZnYb, and BCFZnYb@NPs powders: (a) O 1s and (b) Co 2p. (c) O_2-TPD plots of three samples between room temperature (RT) and 650 °C. (d) TG curves between RT and 1000 °C for three samples. (e) O_2-ECR curves recorded at 600 °C during transition from Ar to air. (f) D_{chem} and k_{chem} of three samples at 600 °C, derived from O_2-ECR fitting, with error bars indicating standard deviation of three independent measurements. (g) H_2O-ECR curves recorded at 600 °C during transition from dry air to wet air. (h) Electronic conductivity of three samples, with error bars indicating standard deviation of three independent measurements. (i) CO_2-TPD plots of three samples between RT and 800 °C.

清華大学出版社 Tsinghua University Press | SciOpen

modifies the oxygen chemical environment and promotes oxygen vacancy formation within the perovskite lattice, while the dual-phase structure may provide additional interfacial and surface-related contributions to the oxygen exchange behavior.

The oxidation states of multivalent cations in perovskites can also serve as an indirect indicator of the oxygen vacancy concentration. High-resolution XPS spectra of Co 2p and Fe 2p (Figs. 2(b) and S7 in the ESM) reveal notable differences in redox behavior among the three systems, demonstrating that Zn/Yb codoping drives electronic reconstruction within the perovskite lattice through redistribution of cation valence states. Compared to BCFZY (Co^{3+}: 68.0%, Fe^{2+}: 37.9%), single-phase BCFZnYb exhibits increased proportions of Co^{3+} (74.5%) and Fe^{2+} (43.4%), corresponding to increases of 9.5% and 14.5%, respectively. The dual-phase BCFZnYb@NPs exhibit an even greater increase in Fe^{2+} content (46.4%, +22.4%) but a smaller rise in Co^{3+} (73.8%, +8.5%) [30–32]. This discrepancy may be related to the presence of the $BaCoO_{3-\delta}$ secondary phase identified by Rietveld refinement [33]. In addition to the aforementioned lower average oxidation states of Co and Fe, the substitution of Zr^{4+} with lower-valent Zn^{2+} further reduces the average B-site valence in Zn/Yb-doped oxides. According to the charge compensation principle, a lower B-site cationic charge promotes oxygen vacancy formation, as each oxygen vacancy effectively carries a +2 charge to maintain electroneutrality [34]. The decreased oxidation states of Co and Fe cations in Zn/Yb-containing samples are consistent with the reduced O_{lat}/O_{ads} ratio, supporting the enhanced oxygen nonstoichiometry induced by Zn/Yb incorporation and together with additional contributions from the dual-phase structure.

At the operational temperatures of PCFCs, thermal reduction of multivalent B-site cations can lead to lattice oxygen release and mass loss. O_2-TPD profiles (Fig. 2(c)) reveal that the lattice oxygen desorption temperature of BCFZnYb is 92 °C lower than that of BCFZY (342 °C), and the dual-phase BCFZnYb@NPs exhibit a further 35 °C reduction compared to BCFZnYb. This progressive decrease in desorption temperature suggests facilitated lattice oxygen release and weakened metal–oxygen bonding in Zn/Yb codoped oxides, suggesting that the dual-phase structure may further facilitate oxygen exchange and oxygen ion transport. The O_2-TPD profile of BCFZnYb@NPs exhibits multiple desorption features around the main peak at 215 °C, which can be attributed to the diverse oxygen chemical environments in the dual-phase structure. In addition to the main peak associated with bulk lattice oxygen, the shoulder peaks are likely related to lattice oxygen from the $BaCoO_{3-\delta}$ secondary phase and the matrix/nanoparticle interfaces, where these oxygen species exhibit different oxygen–binding environments and desorption behaviors. Consistent with this trend, TG curves recorded up to 1000 °C (Fig. 2(d)) show mass losses of 4.53% for BCFZnYb@NPs and 3.68% for BCFZY, suggesting increased overall oxygen-release behavior during heating.

To further characterize the oxygen-related transport properties of the three materials, O_2-induced electrical conductivity relaxation (O_2-ECR) measurements were conducted at 600 °C (Fig. 2(e)). As shown in Fig. S8 in the ESM, the specimens used for ECR measurements exhibit high densification, ensuring that the measured relaxation kinetics reflect intrinsic transport properties. The results show that BCFZnYb@NPs have the fastest kinetic response, followed by BCFZnYb and BCFZY. This trend is consistent with the gradient in the oxygen vacancy concentration derived from earlier analyses. Quantitative fitting of triplicate measurements of O_2-ECR kinetics (Fig. 2(f)) yields the bulk diffusion coefficient (D_{chem}) and surface exchange constant (k_{chem}) at 600 °C, both of which increase in the order BCFZY < BCFZnYb < BCFZnYb@NPs. Error bars in Fig. 2(f) represent the standard deviation of the three independent measurements. This trend suggests that Zn/Yb codoping enhances ionic transport through a vacancy-mediated pathway, while the exsolved secondary phase may additionally contribute to surface oxygen exchange and interfacial transport processes. Figure 2(g) shows the H_2O-induced electrical conductivity relaxation (H_2O-ECR) curves, and the corresponding D_{chem} and k_{chem} values at 600 °C are summarized in Fig. S9 in the ESM. BCFZY exhibits a D_{chem} of 2.17×10^{-6} $cm^2\cdot s^{-1}$ and a k_{chem} of 1.00×10^{-4} $cm\cdot s^{-1}$. For BCFZnYb, D_{chem} and k_{chem} increase to 2.85×10^{-6} $cm^2\cdot s^{-1}$ and 1.7×10^{-4} $cm\cdot s^{-1}$, representing improvements of 31.4% and 70.0%, respectively. BCFZnYb@NPs show further enhancement, with D_{chem} reaching 5.29×10^{-6} $cm^2\cdot s^{-1}$ and k_{chem} reaching 2.8×10^{-4} $cm\cdot s^{-1}$, corresponding to increases of 143.8% and 180.0% relative to BCFZY. These results demonstrate that BCFZnYb@NPs significantly enhance the chemical diffusion and surface exchange kinetics in H_2O-containing atmospheres compared with BCFZY, suggesting improved hydration-related transport behavior [35].

Electronic conductivities of the three materials, measured by a four-probe DC method from triplicate measurements, exhibit the Arrhenius-type behavior characteristic of thermally activated semiconductors (Fig. 2(h)). Error bars in Fig. 2(h) represent the standard deviation of the three independent measurements. Across the entire operating temperature range of 300–800 °C, BCFZnYb@NPs demonstrate higher electronic conductivity than BCFZY. Notably, BCFZnYb shows the highest conductivity among the three materials. This is attributed to the reduced electron scattering in its single-phase structure compared to the oxygen vacancy-rich dual-phase BCFZnYb@NPs. Such enhanced electronic conductivity is crucial for triple-conducting PCFC cathodes, as it promotes interfacial charge transfer during the ORR.

The inevitable presence of CO_2 in practical PCFC operating environments poses a critical challenge to the long-term stability of air electrodes, primarily due to the reaction between alkaline–earth elements (e.g., Ba) in the perovskite and CO_2, forming insulating carbonates that block active sites and degrade ORR activity. To evaluate the CO_2 interaction behavior, CO_2-temperature-programmed desorption (CO_2-TPD) was conducted. As shown in Fig. 2(i), BCFZnYb@NPs exhibit a markedly reduced desorption peak area associated with moderate-strength basic sites compared to BCFZY, indicating enhanced CO_2 tolerance from the Zn/Yb codoping strategy. This effect is further enhanced by the reduced Ba content in the primary perovskite phase due to the introduction of Zn and Yb. In addition, BCFZnYb@NPs show attenuated intensity in high-temperature desorption regions corresponding to strong basic sites, which are prone to strong CO_2 adsorption and irreversible carbonate formation [36]. The desorption temperature of these strong basic sites decreases from 702.5 °C (BCFZY) to 663.2 °C (BCFZnYb@NPs), indicating that even when the active sites interact with CO_2, the adsorption remains more reversible and is less likely to form stable carbonate species [37,38]. XRD patterns acquired for the three electrodes before and after exposure to flowing 1% CO_2 at 550 °C for 24 h further support the improved CO_2 tolerance of the Zn/Yb codoped electrodes (Fig. S10 in the ESM). Both co-doped electrodes show significantly smaller shifts in their main diffraction peaks compared to BCFZY, confirming their improved structural and chemical stability under CO_2-containing environments. However, it should be noted that under this accelerated poisoning condition (Fig. S11 in the ESM), weak $BaCO_3$ diffraction peaks were observed for all three materials. Nevertheless, the differences in peak intensity among the samples

were not sufficiently significant to effectively distinguish their CO_2 tolerance. In contrast, the shifts in the main diffraction peaks induced by the chemical interaction between CO_2 and the perovskite lattice are more sensitive to the intrinsic CO_2 tolerance of the materials, as they more clearly reflect subtle variations in lattice structure and chemical state. Therefore, the shift of the main diffraction peaks was adopted as the primary criterion for evaluating CO_2 tolerance.

To systematically evaluate the synergistic effects of Zn/Yb codoping and $BaCoO_{3-\delta}$ on air electrode performance, electrochemical impedance spectroscopy (EIS) was conducted on symmetric cells with BCFZnYb@NPs, BCFZnYb, and BCFZY electrodes under open-circuit voltage (OCV) in both dry and humidified air atmospheres. To further elucidate the origin of the performance enhancement, DRT analysis was applied to deconvolute the EIS spectra into three processes: a high-frequency (HF, ≥ 10^4 Hz) process associated with ion transfer at the electrolyte–cathode interface, an intermediate-frequency (IF, 1–10^4 Hz) process related to bulk ion transport and surface exchange within the electrode, and a low-frequency (LF, 10^{-2}–1 Hz) process attributed to gas-phase diffusion [39,40]. Under dry air at 600 °C (Fig. 3(a)), DRT analysis reveals that the Zn/Yb codoped electrodes exhibit substantially reduced resistances across all frequency regions, with the dual-phase BCFZnYb@NPs composite achieving the lowest overall R_p. This superior performance is directly linked to the secondary phase, which increases the active site density and accelerates surface exchange reactions. Consistent with this trend, ASR values derived from EIS in the 500–700 °C range are presented in Fig. 3(b). The BCFZnYb@NPs electrode consistently exhibits the lowest ASR across all temperatures, reaching 0.397 Ω·cm² at 600 °C, compared with 0.526 Ω·cm² for BCFZY and 0.443 Ω·cm² for BCFZnYb. These results demonstrate that Zn/Yb codoping significantly enhances ORR activity, with the dual-phase structure providing additional catalytic benefits. The reduction in ASR correlates strongly with increased oxygen vacancy concentration, as established in earlier analyses (Fig. 2(f)).

Under humidified conditions, proton conduction proceeds via the Grotthuss mechanism [34,41,42], in which adsorbed water molecules dissociate at oxygen vacancies to form hydroxyl groups (OH^-), as described by Eq. (2):

$$H_2O + V_O^{\cdot\cdot} + O_O^{\times} = 2OH_O^{\cdot} \quad (2)$$

As shown in Fig. 3(c), in a 3% H_2O-air atmosphere at 600 °C, BCFZnYb@NPs exhibit an R_p value of 0.166 Ω·cm², representing a 32.3% reduction compared to BCFZY (0.245 Ω·cm²), which is also lower than that of BCFZnYb (0.187 Ω·cm²). The DRT results under humidified conditions (Fig. 3(d)) indicate that

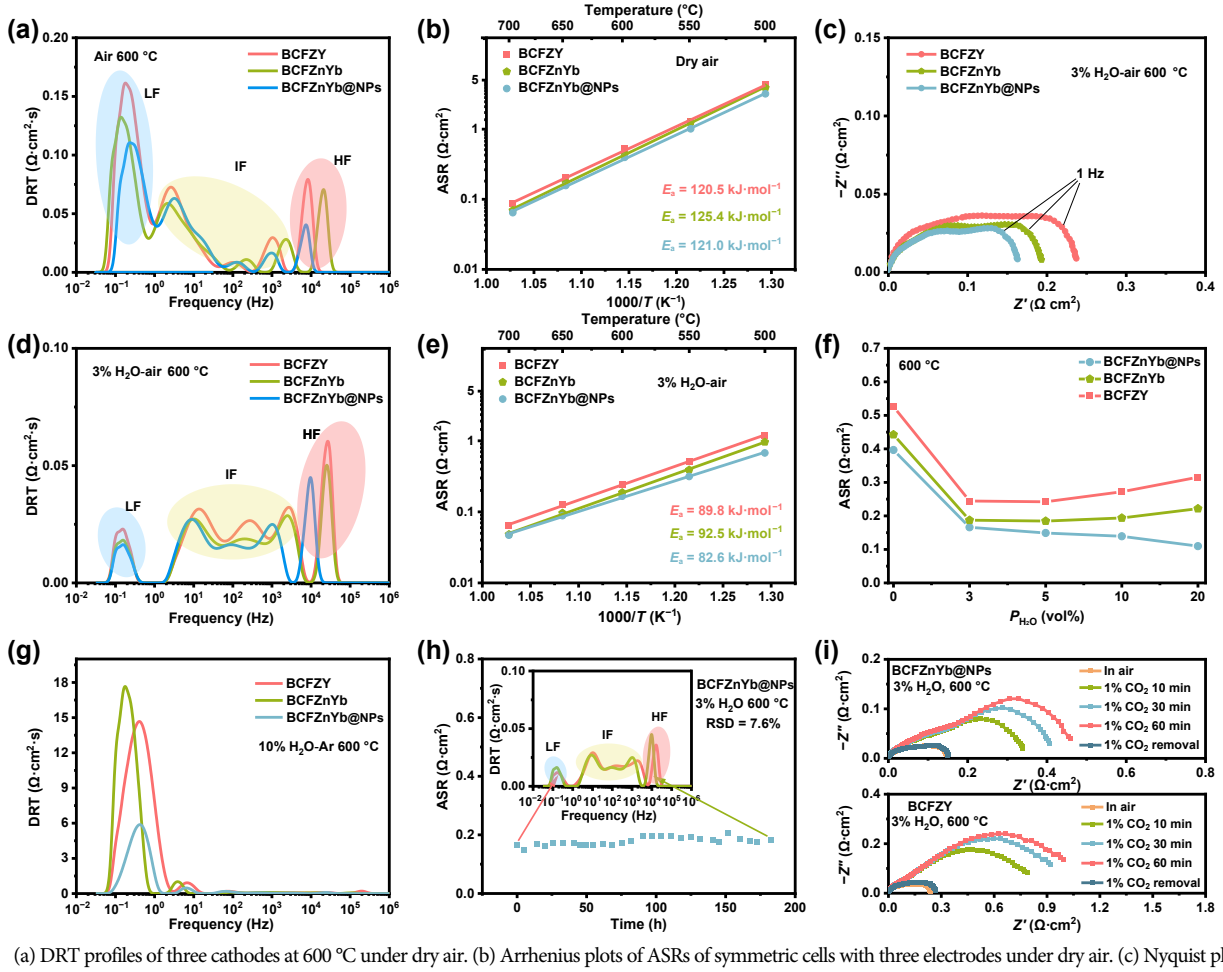


Fig. 3 (a) DRT profiles of three cathodes at 600 °C under dry air. (b) Arrhenius plots of ASRs of symmetric cells with three electrodes under dry air. (c) Nyquist plots of three electrodes measured from symmetric cell under 3% H_2O-air at 600 °C. (d) DRT profiles of three cathodes at 600 °C under 3% H_2O-air. (e) Arrhenius plots of ASRs of symmetric cells with three electrodes under 3% H_2O-air. (f) Impact of humidity (0–20% H_2O-air) on ASR of symmetric cells featuring three distinct electrodes. (g) DRT functions of three electrodes under 10% H_2O-Ar at 600 °C. (h) ASRs of symmetric cell with BCFZnYb@NPs electrode as a function of time tested in 3% H_2O-air at 600 °C, with inset showing DRT curves corresponding to EIS spectra at beginning and end of stability test. (i) BCFZnYb@NPs and BCFZY symmetric cells tested at 600 °C for transition from air to CO_2 and finally back to air.

BCFZnYb@NPs have reduced resistance across all frequency domains, suggesting that their dual-phase structure synergistically facilitates multiple reaction steps, including gas diffusion, oxygen dissociation/adsorption, and ion transport. Compared with the DRT analysis under dry air, the low- and intermediate-frequency resistances are significantly reduced under humidified conditions, which is attributed to the introduction of proton-involved transport processes and enhanced surface reaction kinetics in the presence of H_2O. This process extends the reaction zone from the electrolyte/electrode interface to the entire electrode, thereby accelerating surface charge-transfer kinetics [43,44]. Arrhenius plots of ASR (Figs. 3(b) and 3(e)) reveal that although all three electrodes show comparable activation energies under dry conditions, the dual-phase BCFZnYb@NPs exhibit a significantly lower activation energy in humidified air. The pronounced reduction in the apparent electrode-reaction activation energy under humidified conditions suggests the contribution of hydration-related proton transport to the overall electrode reaction kinetics, which is consistent with the triple-conducting characteristics of the material [45]. The influence of humidity on electrode performance was further investigated by measuring R_p values under varying moisture levels (Fig. 3(f)). The R_p of BCFZnYb@NPs continuously decreases as the H_2O content increases up to 20%, whereas both BCFZnYb and BCFZY display initial improvement followed by degradation beyond 5% H_2O. This behavior is attributed to the enhanced hydration-related transport behavior of BCFZnYb@NPs. XPS, O_2-TPD, TG, and H_2O-ECR results reveal its high oxygen vacancy concentration and rapid bulk diffusion capability, which provide abundant active sites for continuous H_2O incorporation and hydration reactions. The shortened relaxation time observed in H_2O-ECR indicates faster hydration-related transport kinetics in BCFZnYb@NPs. As a result, the detrimental effects commonly associated with excessive H_2O exposure, such as surface-site blocking and hindered oxygen surface exchange, are effectively alleviated within the investigated humidity range. Furthermore, this is corroborated by the DRT analysis of EIS spectra measured in an Ar atmosphere containing 10% H_2O (Fig. 3(g)). Compared with the conventional triple-conducting cathode BCFZY, BCFZnYb@NPs exhibit a smaller low-frequency peak, indicating less hindered gas diffusion under 10% H_2O conditions and more efficient hydration-related charge transport within the electrode. Such enhanced hydration-related electrochemical behavior enables the material to tolerate higher H_2O concentrations in air.

To evaluate hydrothermal stability, BCFZnYb@NPs, BCFZnYb, and BCFZY electrodes were treated at 550 °C under flowing water vapor for 24 h. As revealed in Fig. S12 in the ESM, XRD analysis shows that the (110) diffraction peaks shift to higher diffraction angles by 0.14° for BCFZnYb and 0.13° for BCFZY, corresponding to lattice contractions of Δd = 0.027 and 0.024 Å, respectively. In contrast, the dual-phase BCFZnYb@NPs show a smaller shift of only 0.09° (Δd = 0.011 Å), indicating that the dual-phase structure alleviates lattice distortion through synergistic interfacial stabilization. Long-term stability testing of BCFZnYb@NPs symmetric cells at 600 °C in 3% H_2O-air (Fig. 3(h)) shows less than 10% variation in ASR over 180 h, as determined by the relative standard deviation (RSD). DRT analysis of aged samples reveals a negligible change in the IF range for BCFZnYb@NPs, indicating that the dual-phase electrode maintains high surface exchange activity and structural integrity without significant degradation from hydrothermal corrosion [46].

In addition to hydrothermal stability, CO_2 poisoning represents another critical challenge to the long-term durability of PCFCs [9,47]. To evaluate the CO_2 tolerance of the three electrode systems (Figs. 3(i) and Fig. S13 in the ESM), symmetric cells were operated in humidified air containing 1% CO_2, with periodic EIS measurements used to track the impedance evolution. After CO_2 removal and a 60 min recovery period, both BCFZnYb@NPs and BCFZnYb electrodes nearly regain their original impedance spectra, whereas the BCFZY electrode fails to return to its initial state. As shown in Fig. S14 in the ESM, quantitative analysis of the ASR increase reveals that BCFZnYb exhibits the smallest ASR variation among the three samples, suggesting that the presence of the Ba-rich secondary phase may slightly compromise the CO_2 tolerance. Nevertheless, the overall CO_2 resistance of BCFZnYb@NPs remains significantly superior to that of BCFZY.

The electrochemical performance of single cells employing BCFZY, BCFZnYb, and BCFZnYb@NPs as cathodes was

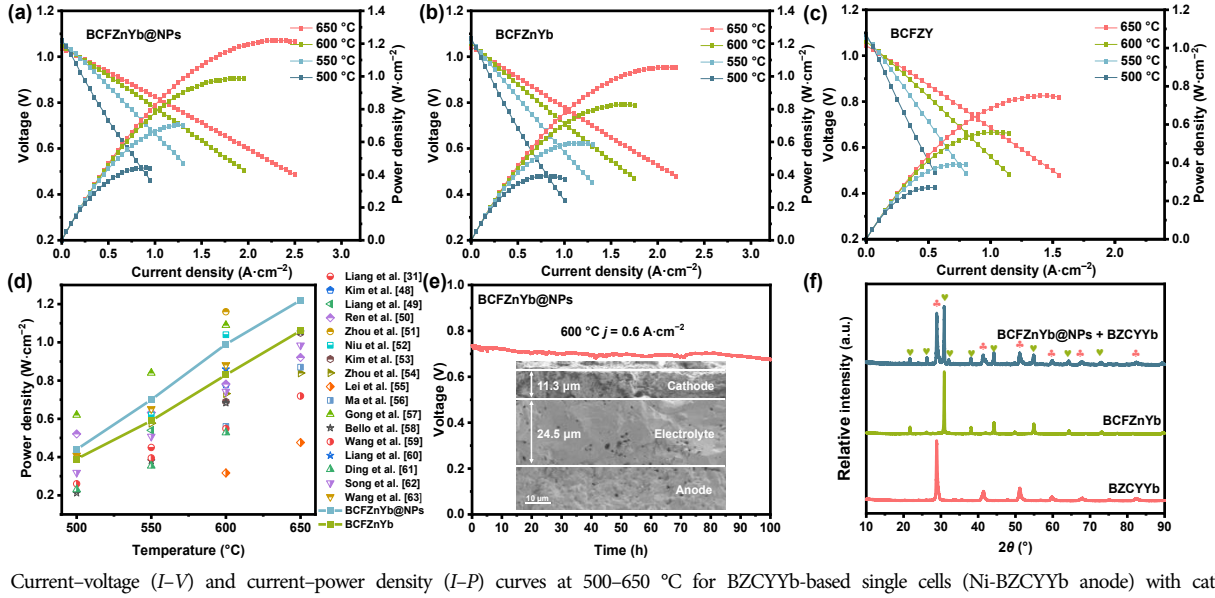


Fig. 4 Current–voltage (*I*–*V*) and current–power density (*I*–*P*) curves at 500–650 °C for BZCYYb-based single cells (Ni-BZCYYb anode) with cathodes: (a) BCFZnYb@NPs, (b) BCFZnYb, and (c) BCFZY. (d) PPDs of BCFZnYb@NPs composite cathode, BCFZnYb cathode, and some other recently reported cathodes. (e) Long-term durability of BCFZnYb@NPs-based single cell operated at 600 °C under a constant current density of 0.6 A·cm^{-2} and SEM image of the BCFZnYb@NPs-based single cell. (f) XRD patterns of BCFZnYb@NPs cathode, BZCYYb electrolyte, and their composite after calcination at 950 °C for 2 h in air.

systematically investigated. As shown in Figs. 4(a)–4(c), the cell with the dual-phase BCFZnYb@NPs cathode exhibits peak power densities (PPDs) of 1.22, 0.99, 0.70, and 0.44 W·cm^{-2} at 650, 600, 550, and 500 °C, respectively. These values substantially exceed those of the BCFZY-based cell (0.75, 0.56, 0.39, and 0.27 W·cm^{-2}) and the single-phase BCFZnYb cell, which exhibits intermediate PPDs of 1.06, 0.83, 0.59, and 0.39 W·cm^{-2} under identical conditions. Notably, the performance advantage of BCFZnYb@NPs is particularly pronounced at lower temperatures, achieving a 63.1% higher PPD at 500 °C compared to the BCFZY baseline (0.442 vs. 0.271 W·cm^{-2}). To further illustrate these performance improvements, Fig. 4(d) benchmarks these PPDs against recently reported representative PCFC cathodes over the temperature range of 500–650 °C [31,48–63]. For improved comparability, Table S1 summarizes the key testing conditions of all referenced studies, including electrolyte type, cell configuration, and operating atmospheres. The results confirm that the BCFZnYb@NPs cathode achieves excellent power output in comparable proton ceramic fuel cell systems. In addition, the cell with the BCFZnYb@NPs cathode maintains stable operation for over 100 h at 600 °C and a current density of 0.6 A·cm^{-2} (Fig. 4(e)), with a degradation rate of only 0.091% h^{-1}, demonstrating excellent long-term durability. As shown in Fig. S15 in the ESM, the evolution of the area-specific resistance (ASR) measured at selected time intervals under open-circuit voltage indicates that the BCFZnYb@NPs cathode maintains a low ASR throughout the entire testing period without noticeable performance degradation. As shown in Fig. S16 in the ESM, SEM characterization of the cathode layer after the single-cell stability test revealed no obvious agglomeration or coarsening of the nanoparticles on the BCFZnYb@NPs surface. In addition, the XRD patterns of BCFZnYb@NPs after sintering at 600 °C for 100 h (Fig. S17 in the ESM) indicate that the secondary phase remained stable, while no evident phase separation was observed in the primary phase. Given that interfacial reactions and elemental interdiffusion between the electrode and electrolyte can lead to the formation of deleterious secondary phase-degrading charge transfer kinetics and increasing polarization losses, the chemical compatibility of the BCFZnYb@NPs cathode with the BZCYYb electrolyte was thoroughly evaluated. XRD analysis of mixed powders (BCFZnYb@NPs + BZCYYb) calcined at 950 °C for 2 h (Fig. 4(f)) shows that both materials retain their distinct crystal structures, indicating excellent chemical compatibility without detectable reactive interdiffusion.

To elucidate the roles of Zn/Yb in oxygen vacancy formation, ionic transport, and charge transfer, DFT calculations were performed on the host lattice of BCFZnYb@NPs without the secondary phase (denoted as BCFZnYb@NPs-H), along with bulk BCFZnYb and BCFZY models (Fig. S18 in the ESM). As shown in Figs. 5(a) and 5(b), the charge density distributions reveal a pronounced shift of electron density from oxygen atoms toward Zn centers in BCFZnYb@NPs-H. This behavior stems from the

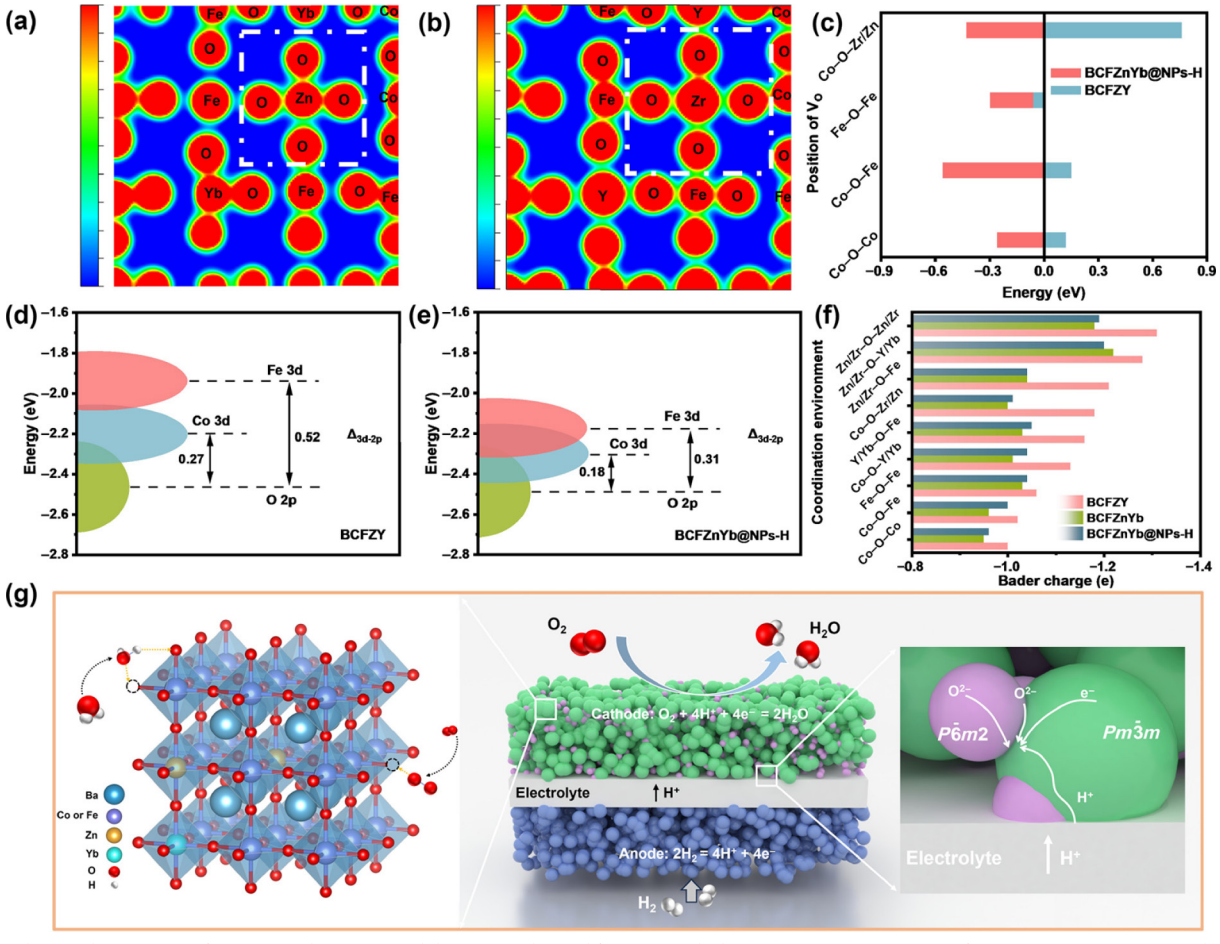


Fig. 5 Electron density maps of (a) BCFZnYb@NPs-H and (b) BCFZY obtained from DFT calculations. (c) Formation energy of oxygen vacancies in BCFZnYb@NPs-H and BCFZY determined using DFT calculations. Schematic illustration of Co–O and Fe–O bond covalency for (d) BCFZY and (e) BCFZnYb@NPs-H. (f) Bader charges of oxygen atoms in different coordination environments for BCFZY, BCFZnYb, and BCFZnYb@NPs-H. (g) Schematic diagrams of single cell with dual-phase BCFZnYb@NPs cathode, its microstructure, and its crystal structure.

higher electronegativity of Zn relative to Zr, which strengthens Zn–O covalency and promotes electron delocalization. The electron-withdrawing nature of Zn reduces the electron density on neighboring oxygen atoms, and this electronic redistribution polarizes the oxygen sites, effectively reducing their anionic character and weakening electrostatic interactions with adjacent B-site cations [64]. Consequently, this bond destabilization lowers ΔE_v and enhances oxygen-ion mobility, thereby significantly improving oxygen-ion conduction at elevated temperatures—a finding consistent with earlier O_2-ECR results (Fig. 2(f)). As presented in Fig. 5(c), the DFT-derived ΔE_v values for BCFZnYb@NPs-H are consistently lower than those for BCFZY in all representative metal–oxygen–metal configurations (e.g., Co–O–Fe, Fe–O–Fe), confirming that Zn/Yb doping markedly facilitates oxygen vacancy formation.

To further probe the underlying electronic origin, the electronic structures of the three cathode materials were analyzed. As shown in Fig. S19 in the ESM, the total density of states (TDOS) near the Fermi level exhibits differences among the three compositions. The TDOS of BCFZnYb@NPs-H exhibits more electronic states in the vicinity of the Fermi level, suggesting a higher density of accessible electronic states and enhanced carrier delocalization, both of which are favorable for electronic transport. Projected density of states (PDOS) analyses (Fig. S20 in the ESM) further reveal that the states in the vicinity of the Fermi level are predominantly derived from strongly hybridized O 2p and transition-metal 3d orbitals. The O 2p band extends continuously from approximately −6 eV to the Fermi level and substantially overlaps with both Co 3d and Fe 3d states, evidencing pronounced d–p hybridization within the perovskite framework [65].

To quantify the degree of orbital coupling, the orbital center positions were extracted. As shown in Figs. 5(d), 5(e), and Fig. S21 in the ESM, the energy-level difference between the Fe 3d and O 2p orbital centers in BCFZY is approximately 0.52 eV, whereas that between the Co 3d and O 2p orbital centers is 0.27 eV. In BCFZnYb@NPs-H, these values decrease to 0.31 and 0.18 eV, respectively. The reduced 3d–2p orbital-center difference reflects strengthened orbital coupling between oxygen and transition-metal cations, consistent with enhanced metal–oxygen covalency and a higher degree of electron delocalization. Additional support is provided by the Bader charge analysis (Fig. 5(f) and Table S2). Oxygen atoms in BCFZnYb@NPs-H generally carry less negative charge than those in BCFZY, implying suppressed electron localization on oxygen and a more covalent metal–oxygen bonding environment. This effect is particularly evident in heterometallic coordination motifs such as Zn–O–Fe and Co–O–Zn, where the electron density around oxygen decreases most significantly. The combination of weakened electrostatic binding and reinforced d–p hybridization is therefore expected to simultaneously promote oxygen mobility and electronic conduction. These results suggest that Zn/Yb codoping induces significant electronic redistribution and weakens electrostatic metal–oxygen interactions. The combined effects of reduced electrostatic attraction and enhanced orbital hybridization promote both lattice oxygen mobility and electronic conduction, providing a fundamental explanation for the enhanced electrochemical performance. These theoretical insights align well with the results of the four-point probe conductivity measurements. As illustrated in Fig. 5(g), oxygen vacancies play essential roles in both electrode hydration and ORR kinetics [66–68]. The Zn/Yb codoped BCFZnYb@NPs system achieves superior catalytic performance through its self-assembled dual-phase structure, in which abundant oxygen vacancies and optimized interfacial charge transfer act synergistically to accelerate the ORR pathway.

4 Conclusions

This work develops a self-assembled dual-phase BCFZnYb@NPs cathode via synergistic Zn/Yb B-site co-doping combined with temperature-induced exsolution under an optimal thermal window. Structural analysis reveals a cubic perovskite matrix decorated with thermally induced hexagonal $BaCoO_{3-\delta}$ nanoparticles, increasing the density of electrocatalytically active sites. Zn/Yb codoping introduces cation-driven charge modulation, increasing the oxygen vacancy concentration while lowering their formation and migration energies, thereby enhancing surface exchange and bulk diffusion. DFT calculations confirm that optimized charge distribution and weakened metal–oxygen bonds reduce the oxygen vacancy formation energy, while enhanced d–p orbital hybridization improves electronic conductivity. These effects accelerate ORR kinetics: the ASR reaches 0.166 Ω·cm² in 3% H_2O-air and decreases to 0.110 Ω·cm² in 20% H_2O-air at 600 °C. A single cell based on this cathode and a BZCYYb electrolyte delivers a peak power density of 0.99 W·cm^{-2} at 600 °C and stable operation over 100 h at 0.6 A·cm^{-2}, along with excellent hydrothermal stability. Meanwhile, the regulation of alkaline–earth sites enhances CO_2 tolerance. This work provides a feasible strategy for the synergistic optimization of activity, conductivity, and stability in PCFC cathodes, offering important guidance for advancing intermediate-temperature PCFCs toward practical applications.

Acknowledgements

This work was supported by the National Key R&D Program of China (No. 2021YFA1501900). This work was financially supported by the National Key R&D Program of China (Nos. 2024YFE0101500 and 2026YFE0151900), the China Postdoctoral Science Foundation (Nos. S202418001/198 and 2025M780002), and the Scientific Research Foundation of Education Department of Anhui Province (No. 2025AHGXZK40238). The authors acknowledge the support from Prof. Yu Liu, which is associated with the National Natural Science Foundation of China (No. 52202324) and the independently funded research project (No. E3550101) of the Nanjing Future Energy System Research Institute, Chinese Academy of Sciences (CAS).

Author contributions

Mengen Shao: Conceptualization, Data curation, Formal analysis, Investigation, Methodology, Validation, Visualization, Writing—original draft, Writing—review & editing; Xinyu Zhao: Formal analysis, Resources, Software; Chaowei Tang: Formal analysis, Investigation; Yuling Yuan: Formal analysis, Investigation; Guangming Yang: Resources, Software; Yan Chen: Funding acquisition, Resources, Software; Jaroslaw Milewski: Resources, Software; Tao Hong: Resources, Software; Yu Liu: Funding acquisition, Resources, Software; Zuoqing Liu: Conceptualization, Funding acquisition, Project administration, Resources, Supervision, Writing—review & editing; Youmin Guo: Conceptualization, Formal analysis, Funding acquisition, Project administration, Resources, Supervision, Writing—review & editing.

Availability of data and materials

The data that support the findings of this study are available from the corresponding author upon reasonable request.

Competing interests

The authors have no competing interests to declare that are relevant to the content of this article.

Electronic Supplementary Material

Supplementary material is available in the online version of this article at https://doi.org/10.26599/JAC.2026.9221340.

References

[1] Dunn B, Kamath H, Tarascon JM. Electrical energy storage for the grid: A battery of choices. *Science* 2011, **334**: 928–935.

[2] Boldrin P, Brandon NP. Progress and outlook for solid oxide fuel cells for transportation applications. *Nat Catal* 2019, **2**: 571–577.

[3] Zhang Y, Chen B, Guan DQ, *et al.* Thermal-expansion offset for high-performance fuel cell cathodes. *Nature* 2021, **591**: 246–251.

[4] Kim S, Yoon D, Chae J, *et al.* Elucidating the proton-coupled oxygen reduction pathway in protonic ceramic fuel cells. *Energ Environ Sci* 2026, **19**: 1715–1731.

[5] Fu M, Hu WJ, Tong H, *et al.* Sn-doped cobalt containing perovskite as the air electrode for highly active and durable reversible protonic ceramic electrochemical cells. *J Adv Ceram* 2024, **13**: 63–72.

[6] Yang S, Yin YR, Boulfrad S, *et al.* Synergistic doping in proton-conducting oxides unlocks high conductivity and low proton trapping. *Adv Funct Mater* 2026, **36**: 74539.

[7] Cao JF, Ji YX, Shao ZP. Perovskites for protonic ceramic fuel cells: A review. *Energ Environ Sci* 2022, **15**: 2200–2232.

[8] Duan CC, Kee RJ, Zhu HY, *et al.* Highly durable, coking and sulfur tolerant, fuel-flexible protonic ceramic fuel cells. *Nature* 2018, **557**: 217–222.

[9] Feng DS, Li M, Peterson VK, *et al. In situ* formation of a melt-solid interface toward stable oxygen reduction in protonic ceramic fuel cells. *Adv Funct Mater* 2025, **35**: 2417425.

[10] Shi N, Xie Y, Tadé MO, *et al.* Evolution and reconstruction of air-electrode surface composition in reversible protonic ceramic cells: Mechanisms, impacts on catalytic performance, and optimization strategies—A review. *Adv Mater* 2025, **37**: 2416528.

[11] Peng CC, Han X, Song JN, *et al.* Electronic modulation strategy via high-valence heteroatom substitution toward high-performance protonic ceramic fuel cell air electrodes. *Appl Catal B-Environ* 2026, **381**: 125829.

[12] Zhao SC, Ma WJ, He BB, *et al.* Single-atom enables reverse hydrogen spillover for high-performance protonic ceramic fuel cells. *Adv Mater* 2025, **37**: 2501387.

[13] Tang SR, Fu M, Qin ZH, *et al.* Topological ion optimized composite cathode for proton-conducting solid oxide fuel cells. *Adv Funct Mater* 2025, **35**: 2501995.

[14] Liu ZQ, Qiao RX, Feng DS, *et al.* Strategic atomic trapping at heterointerfaces for protonic ceramic cells. *Nat Commun* 2025, **16**: 10405.

[15] Gong JY, Du KP, Jiang W, *et al.* Controlled growth of $Pr_{1.5}Ba_{1.5}Cu_3O_7$ cubes to meliorate the cathode reaction for protonic ceramic fuel cells. *J Adv Ceram* 2025, **14**: 9221060.

[16] Yao PH, Zhang J, Qiu QY, *et al.* Enhancing oxygen reduction kinetics and proton transfer of $La_{0.6}Sr_{0.4}Co_{0.2}Fe_{0.8}O_{3-\delta}$ cathode through $Pr_2Ni_{0.5}Co_{0.5}O_{4-\delta}$ impregnation for protonic ceramic fuel cells. *Adv Energy Mater* 2025, **15**: 2403335.

[17] Zamudio-García J, Chiabrera F, Losilla ER, *et al.* Vertical heterostructures for symmetrical and reversible solid oxide fuel cells. *Nano Energy* 2024, **131**: 110293.

[18] Qi HY, Zhao Z, Tu BF, *et al.* Reaction tuned formation of hierarchical $BaCo_{0.4}Fe_{0.4}Zr_{0.1}Y_{0.1}O_{3-\delta}$ cathode. *J Power Sources* 2020, **455**: 227971.

[19] Park K, Saqib M, Lee H, *et al.* Water-mediated exsolution of nanoparticles in alkali metal-doped perovskite structured triple-conducting oxygen electrocatalysts for reversible cells. *Energ Environ Sci* 2024, **17**: 1175–1188.

[20] Cui JZ, Zhang YX, Liu Z, *et al.* Key roles of initial calcination temperature in accelerating the performance in proton ceramic fuel cells via regulating 3D microstructure and electronic structure. *Small Struct* 2024, **5**: 2300439.

[21] Schichlein H, Müller AC, Voigts M, *et al.* Deconvolution of electrochemical impedance spectra for the identification of electrode reaction mechanisms in solid oxide fuel cells. *J Appl Electrochem* 2002, **32**: 875–882.

[22] Kresse G, Furthmüller J. Efficiency of *ab-initio* total energy calculations for metals and semiconductors using a plane-wave basis set. *Comp Mater Sci* 1996, **6**: 15–50.

[23] Kresse G, Furthmüller J. Efficient iterative schemes for *ab initio* total-energy calculations using a plane-wave basis set. *Phys Rev B* 1996, **54**: 11169–11186.

[24] Perdew JP, Burke K, Ernzerhof M. Generalized gradient approximation made simple. *Phys Rev Lett* 1996, **77**: 3865–3868.

[25] Kresse G, Joubert D. From ultrasoft pseudopotentials to the projector augmented-wave method. *Phys Rev B* 1999, **59**: 1758–1775.

[26] Zhu K, Zhang LJ, Shi N, *et al.* A superior catalytic air electrode with temperature-induced exsolution toward protonic ceramic cells. *ACS Nano* 2024, **18**: 5141–5151.

[27] Zhao SC, Ma WJ, Wang WW, *et al.* Reverse atom capture on perovskite surface enabling robust and efficient cathode for protonic ceramic fuel cells. *Adv Mater* 2024, **36**: 2405052.

[28] Wang W, Zhang XZ, Khan K, *et al.* Enhanced ORR activity of A-site deficiency engineered $BaCo_{0.4}Fe_{0.4}Zr_{0.1}Y_{0.1}O_{3-\delta}$ cathode in practical YSZ fuel cells. *Int J Hydrogen Energ* 2021, **46**: 5593–5603.

[29] Zeng DP, Zhu F, Xu K, *et al.* Nb-doped $PrBa_{0.8}Ca_{0.2}Co_2O_6$-based perovskite cathode with improved oxygen reduction reaction activity and stability for solid oxide fuel cells. *J Adv Ceram* 2024, **13**: 1590–1599.

[30] Chen WW, Zou J, Shan L, *et al.* An amperometric high-temperature ammonia sensor based on a $BaCo_{0.4}Fe_{0.4}Zr_{0.1}Y0.1O_{3-\delta}$ triple conductor. *Sensor Actuat B-Chem* 2024, **414**: 135940.

[31] Liang MZ, He F, Zhou C, *et al.* Nickel-doped $BaCo_{0.4}Fe_{0.4}Zr_{0.1}Y_{0.1}O_{3-\delta}$ as a new high-performance cathode for both oxygen-ion and proton conducting fuel cells. *Chem Eng J* 2021, **420**: 127717.

[32] Tao HL, Chen GX, Zhang QJ, *et al.* $BaCo_{0.4}Fe_{0.4}Ce_{0.1}Gd_{0.1}O_{3-\delta}$ as positive electrode for reversible protonic ceramic cells. *J Power Sources* 2025, **636**: 236561.

[33] Chin YY, Hu Z, Lin HJ, *et al.* Spin-orbit coupling and crystal-field distortions for a low-spin $3d^5$ state in $BaCoO_3$. *Phys Rev B* 2019, **100**: 205139.

[34] Guo SH, Jiang LL, Li YF, *et al.* From electrolyte and electrode materials to large-area protonic ceramic fuel cells: A review. *Adv Funct Mater* 2024, **34**: 2304729.

[35] Zhou L, Yin YR, Nematov D, *et al.* A high-performance cobalt-free cathode for proton-conducting solid oxide fuel cells via multi-element doping in $Sr_2Fe_2O_6$. *Sustain Mater Technol* 2026, **48**: 01936.

[36] Niu JT, Zhang CX, Liu HY, *et al.* Enhanced performance of oxygen vacancies on CO_2 adsorption and activation over different phases of ZrO_2. *Front Energy* 2023, **17**: 545–554.

[37] Liu S, Liu LB, Yang M, *et al.* Perovskite-socketed FeCoNiCu quaternary alloy nanoparticles for efficient CO_2 reduction in solid oxide electrolyzer. *Chem Eng J* 2025, **519**: 165404.

[38] Zhang Y, Li JB, Xie HP, *et al.* CO_2-induced reconstruction for ORR-enhanced solid oxide fuel cell cathode. *Chem Eng J* 2023, **462**: 142216.

[39] He F, Zhou YC, Hu T, *et al.* An efficient high-entropy perovskite-type air electrode for reversible oxygen reduction and water splitting in protonic ceramic cells. *Adv Mater* 2023, **35**: 2209469.

[40] Liu PY, Yang WX, Li DR, *et al.* Accurate identification and reduction restoration of early-stage anode oxidation in industrial-sized solid oxide fuel cells. *Int J Hydrogen Energ* 2026, **220**: 154175.

[41] Wang N, Hinokuma S, Ina T, *et al.* Incorporation of bulk proton carriers in cubic perovskite manganite driven by interplays of oxygen and manganese redox. *Chem Mater* 2019, **31**: 8383–8393.

[42] Zohourian R, Merkle R, Raimondi G, *et al.* Mixed-conducting perovskites as cathode materials for protonic ceramic fuel cells: Understanding the trends in proton uptake. *Adv Funct Mater* 2018, **28**: 1801241.
[43] Di HS, Liu ZQ, Xiao M, *et al.* Exploring hydration of air electrodes for protonic ceramic cells: A review. *Chem Eng J* 2025, **507**: 160759.
[44] Yu N, Bello IT, Chen X, *et al.* Rational design of ruddlesden–popper perovskite ferrites as air electrode for highly active and durable reversible protonic ceramic cells. *Nano-Micro Lett* 2024, **16**: 177.
[45] Song WH, Dong XC, Yin YR, *et al.* Reviving the activity of Si-contaminated cathodes via chloride anion doping for proton-conducting solid oxide fuel cells. *J Adv Ceram* 2026, **15**: 9221262.
[46] Liu ZQ, Tao MH, Xiao M, *et al.* Direct ammonia protonic ceramic fuel cells through heterogeneous interface engineering. *Chem Catal* 2025, **5**: 101365.
[47] Zou D, Yi YN, Song YF, *et al.* The $BaCe_{0.16}Y_{0.04}Fe_{0.8}O_{3-\delta}$ nanocomposite: A new high-performance cobalt-free triple-conducting cathode for protonic ceramic fuel cells operating at reduced temperatures. *J Mater Chem A* 2022, **10**: 5381–5390.
[48] Kim JH, Hong J, Lim DK, *et al.* Water as a hole-predatory instrument to create metal nanoparticles on triple-conducting oxides. *Energ Environ Sci* 2022, **15**: 1097–1105.
[49] Liang MZ, Zhu YJ, Song YF, *et al.* A new durable surface nanoparticles-modified perovskite cathode for protonic ceramic fuel cells from selective cation exsolution under oxidizing atmosphere. *Adv Mater* 2022, **34**: 2106379.
[50] Ren RZ, Yu XD, Wang ZH, *et al.* Fluorination inductive effect enables rapid bulk proton diffusion in $BaCo_{0.4}Fe_{0.4}Zr_{0.1}Y0.1O_{3-\delta}$ perovskite oxide for high-activity protonic ceramic fuel cell cathode. *Appl Catal B–Environ* 2022, **317**: 121759.
[51] Zhou YC, Zhang WL, Kane N, *et al.* An efficient bifunctional air electrode for reversible protonic ceramic electrochemical cells. *Adv Funct Mater* 2021, **31**: 2105386.
[52] Niu YH, Zhou YC, Zhang WL, *et al.* Highly active and durable air electrodes for reversible protonic ceramic electrochemical cells enabled by an efficient bifunctional catalyst. *Adv Energy Mater* 2022, **12**: 2103783.
[53] Kim J, Sengodan S, Kwon G, *et al.* Triple-conducting layered perovskites as cathode materials for proton-conducting solid oxide fuel cells. *ChemSusChem* 2014, **7**: 2811–2815.
[54] Zhou C, Sunarso J, Song YF, *et al.* New reduced-temperature ceramic fuel cells with dual-ion conducting electrolyte and triple-conducting double perovskite cathode. *J Mater Chem A* 2019, **7**: 13265–13274.
[55] Lei SY, Ma JY, Li WL, *et al.* A self-assembled composite cathode with enhanced activity and stability for protonic ceramic fuel cells. *J Power Sources* 2025, **631**: 236257.
[56] Ma JY, Xu YS, Zhu F, *et al.* An efficient and robust Co-free $BaFeO_3$-based oxygen electrode for protonic ceramic electrochemical cells. *Sustain Mater Technol* 2024, **40**: 00888.
[57] Gong J, Xu LL, Deng RP, *et al.* Multicomponent doping realized superior triple-conducting within cobalt-free Ruddlesden-Popper-type perovskite for proton-conducting fuel cells cathode. *Int J Hydrogen Energ* 2024, **64**: 158–165.
[58] Bello IT, Yu N, Song YF, *et al.* Electrokinetic insights into the triple ionic and electronic conductivity of a novel nanocomposite functional material for protonic ceramic fuel cells. *Small* 2022, **18**: 2203207.
[59] Wang N, Yuan BY, Tang CM, *et al.* Machine-learning-accelerated development of efficient mixed protonic–electronic conducting oxides as the air electrodes for protonic ceramic cells. *Adv Mater* 2022, **34**: 2203446.
[60] Liang MZ, Liu DL, Zhu YJ, *et al.* Nickel doping manipulation toward developing high-performance cathode for proton ceramic fuel cells. *J Electrochem Soc* 2022, **169**: 094509.
[61] Ding HP, Wu W, Jiang C, *et al.* Self-sustainable protonic ceramic electrochemical cells using a triple conducting electrode for hydrogen and power production. *Nat Commun* 2020, **11**: 1907.
[62] Song YF, Chen YB, Wang W, *et al.* Self-assembled triple-conducting nanocomposite as a superior protonic ceramic fuel cell cathode. *Joule* 2019, **3**: 2842–2853.
[63] Wang N, Toriumi H, Sato Y, *et al.* $La_{0.8}Sr_{0.2}Co_{1-x}Ni_xO_{3-\delta}$ as the efficient triple conductor air electrode for protonic ceramic cells. *ACS Appl Energy Mater* 2021, **4**: 554–563.
[64] Hou NJ, Gan JJ, Yan QS, *et al.* Improved electrochemical oxidation kinetics of $La_{0.5}Ba_{0.5}FeO_{3-\delta}$ anode for solid oxide fuel cells with fluorine doping. *J Power Sources* 2022, **521**: 230932.
[65] Liu XY, Song C, Wang ZM, *et al.* High-entropy-tailored d–p orbital hybridization for enhanced oxygen reduction reaction in perovskite air electrodes of solid oxide fuel cells. *Adv Mater* 2026, **38**: 72892.
[66] Chen X, Tan YS, Li Z, *et al.* Advanced air electrodes for reversible protonic ceramic electrochemical cells: A comprehensive review. *Adv Mater* 2025, **37**: 2418620.
[67] Ma JM, Tao ZT, Kou HN, *et al.* Evaluating the effect of Pr-doping on the performance of strontium-doped lanthanum ferrite cathodes for protonic SOFCs. *Ceram Int* 2020, **46**: 4000–4005.
[68] Liu Y, Shao ZP, Mori T, *et al.* Development of nickel based cermet anode materials in solid oxide fuel cells—Now and future. *Mater Rep Energy* 2021, **1**: 100003.